Energy Proceedings
Vol 53, 2025
ISSN 2004-2965

Degradation Prediction Model based on CEEMDAN-LSTM Hybrid Method Considering Reversible Degradation of Proton Exchange Membrane Fuel Cell#

Huijin Guo[1,2], Julong Zhou[1], Jinghui Zhao[1,2], Beiming Huang[1], Ruitao Li[1,*], Tiancai Ma[1,3,**]

1 School of Automotive Studies, Tongji University, Shanghai, 201804, P. R. China

2 AT&M Environmental Engineering Technology Co., Ltd., Beijing 100081, P. R. China

3 Institute of Carbon Neutrality, Tongji University, Shanghai, 200092, P. R. China

(* Corresponding Author: 2010853@tongji.edu.cn.)
(** Corresponding Author: matiancai@tongji.edu.cn.)

ABSTRACT

The demonstration of proton exchange membrane fuel cell (PEMFC) technology for commercial vehicles has shown increasing success, but comprehensive commercialization remains limited by the service life of the cells. Timely prediction of fuel cell lifetime can enhance state assessment in advance, enabling precise control for performance recovery operations, thus reducing use and maintenance costs and avoiding predictable risks. Commonly used lifetime prediction models are categorized into mechanistic models, data-driven models and hybrid models. However, data-driven prediction methods often overlook degradation mechanisms, while mechanistic models lack real-time data integration. Additionally, the incomplete exploration of mathematical degradation mechanisms poses challenges for mechanistic models. The frequent start-stop cycles result in significant voltage recovery phenomena, complicating the accuracy of remaining lifetime predictions. This paper presents accelerated stress tests conducted on a 15kW fuel cell stack under idle, rated, and dynamic load conditions, discussing performance recovery following shutdown periods under various operating conditions. The experimental results indicate significant voltage recovery at all current conditions, with the most pronounced recovery occurring at high current conditions. Voltage recovery increases with longer downtime durations. Additionally, a data-driven model utilizing complete ensemble empirical mode decomposition with adaptive noise (CEEMDAN) and long-short term memory network (LSTM) was proposed. The model first decomposed raw voltage data into modal sequences with distinct characteristic time scales, which were then input into the LSTM for voltage prediction. The prediction results demonstrate that the CEEMDAN-LSTM hybrid model reduces RMSE by 30.41% and 18.21% compared to the LSTM and GRU models under idle conditions, by 28.37% and 16.87% under rated conditions, and by 17.02% and 16.14% under variable load conditions, respectively.

Keywords: proton exchange membrane fuel cell, reversible degradation, degradation prediction, CEEMDAN-LSTM

1. INTRODUCTION

In actual operation, proton exchange membrane fuel cells (PEMFCs) demonstrate a gradual decline in performance over time. This voltage degradation encompasses both a gradual decline due to the intrinsic material degradation of the cell and a rapid decline resulting from failures. Irrespective of the underlying cause, voltage prediction models are capable of forecasting future voltage trends, thereby enabling the control system to make proactive decisions. This provides crucial reference information for maintaining the fuel cell under optimal operating conditions. The aging of fuel cells is a complex and nonlinear process[1]. Additionally, the phenomenon of voltage recovery due to shutdowns, changes in operating parameters changing, purging, and environmental fluctuations[2] further complicate the prediction accuracy of voltage trends in fuel cells[3].

After a period of shutdown, fuel cells often exhibit a voltage recovery phenomenon known as reversible loss[4]. A number of scholars have put forth explanations for the causes of reversible loss and proposed methods for recovery. The formation of oxides on Pt has been demonstrated to reduce the effective catalytic surface area (ECSA), with voltage recovery occurring when these

This is a paper for the 16th International Conference on Applied Energy (ICAE2024), Sep. 1-5, 2024, Niigata, Japan.

oxides are reduced at low potentials[5,6]. Other researches[7–9] has indicated that reversible losses resulting from membrane degradation products can be mitigated by operating at low potentials and increasing the intake gas humidity. Furthermore, water plays a pivotal role in influencing reversible voltage loss. Pawel et al.[10] proposed that reversible losses may be attributed to water accumulation and uneven water content, and they proceeded to develop a linear fitting formula for the reversible decay portion. The majority of current researches[11–14] focus on the timely purging or augmentation gas humidity, with the objective of preventing the effects of flooding or membrane desiccation.

Data-driven and mechanistic models are two commonly used prediction methods[15]. Model-based methods consider the impact of internal degradation factors and external operating conditions on fuel cell performance degradation[15–17], using mechanistic models or empirical formulas to predict the performance decline of fuel cells[18]. Nevertheless, the insufficient study of degradation mechanisms and the considerable impact of environmental and operational conditions on fuel cell performance render the prediction accuracy of purely model-based methods severely limited. While some studies have incorporated data-driven filtering techniques to refine model parameters[19,20], hybrid methodologies remain contingent on fuel cell models, and the filtering algorithms are vulnerable to noise[21]. Moreover, models are unable to accurately represent the reversible degradation phenomena observed in fuel cells. When sufficient lifetime data is available, data-driven methods, as black-box models, can predict outcomes without considering the effects of aging. However, a limitation of this approach is the inability to elucidate the underlying causes of degradation. The most commonly utilized data-driven models include convolutional neural networks (CNN)[22], recurrent neural networks (RNN)[23], gated recurrent units (GRU) [24], support vector machines[25], and echo state networks (ESN)[26] and so on. Long-short term memory (LSTM) network is a commonly utilized approach for addressing time series predictions[27]. However, due to constraints in feature extraction and nonlinear expression, these shallow networks may not adequately address the complex nonlinear degradation data of fuel cells[28]. The application of discrete wavelet transform (DWT) methods can facilitate the precision of voltage data preprocessing, which encompasses the incorporation of highly nonlinear characteristics derived from reversible degradation and anomalous states[29]. The decomposition of data may facilitate the reflection of disparate time scales of degradation[30], yet this approach depends on the judicious selection of wavelet basis functions[28].

For the aforementioned shortcomings in the current state of researches, this paper proposed a hybrid data-driven model that fuses Complete Ensemble Empirical Mode Decomposition with Adaptive Noise (CEEMDAN) and Long Short-Term Memory (LSTM) networks. This model decomposes the aging trends of fuel cells on multiple time scales without the necessity of defining basis functions, then predicts and reconstructs each modal sequence, thereby enhancing the model's voltage prediction performance. Firstly, an accelerated stress test (AST) was conducted on a 15kW fuel cell stack under Idle, Rated, and Dynamic load conditions to investigate the performance recovery after shutdown under different operational conditions. Secondly, the voltage trends under each working condition were predicted by CEEMDAN-LSTM and compared with the traditional single GRU model and the single LSTM model.

2. EXPERIMENTS

2.1 Fuel cell stack

The tested stack was a water-cooled graphite bipolar plate stack with a rated output power of 15 kW and a rated current of 495 A, which was equivalent to 1500 mA cm^{-2}, with a peak output power of 18 kW. Single cell has an active area of 330 cm^2, with a cathode catalyst layer platinum loading of 0.4 mg cm^{-2} and an anode catalyst layer platinum loading of 0.07 mg cm^{-2}. The commercial proton exchange membrane (obtained from *Tangfeng Energy Technology Co., LTD*. C081 model products) had a thickness of 39 microns. The H_2 and air were introduced in a counter-flow configuration, with the coolant flowing in the same direction as the air intake. The stack comprised 46 cells in series. Cell voltage monitor (CVM) module was arranged 1 inspection channel for every 2 cells, with a total of 23 voltage acquisition channels. The voltage of each cell was calculated using the differential method.

2.2 Testbench

The YK-C20 test bench, manufactured by *Dalian Yuke Innovation Technology Co., LTD*, comprises a gas supply system, thermal management system, load system, control system, and data acquisition system. The test power range is 0 ~ 30 kW, with sensor signals from the test system recorded at 1000ms intervals. The configuration of the test bench is illustrated in Figure 1.

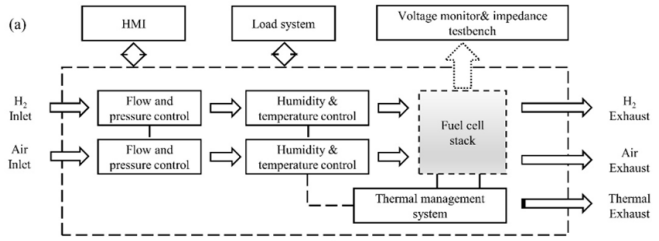

Fig. 1. Structural diagram of test bench.

2.3 AST protocol

The AST protocol for the stack was based on the Chinese national standard *GB/T38914-2020 Evaluation Method for Lifetime of Proton Exchange Membrane Fuel Cell Stack in Vehicle Application*. The AST included Idle condition, Rated condition, and Dynamic load condition. The cyclic test processes for each test condition are delineated in Table 1-3 and conducted in accordance with the procedures illustrated in Fig.2. Each test condition comprised 13 cycles, designated as NO. 1-13 AST-Idle (Rated, Dynamic) in sequential order. Each AST cycle comprised a series of smaller cycles, designated as secondary cycles. For instance, each AST-Idle cycle encompassed four secondary cycles. The duration of each AST cycle was four hours, plus the intermediate downtime, resulting in a total experimental duration exceeding 64 hours for each test condition.

Table 1. AST procedure of idle condition.

Step	Condition	Parameters
1	Start	Precondition: Voltage of single cell < 0.3 V
		Maintained current: 66A
2	Idle current	Start timing
		Operating current 66A
3	Reference current	Load from 66A to 462A every 1 hour intervals, hold for 90s and record voltage, then unload to 66A
4	Stop	Precondition: 4h of continuous operation at 66A and 462A
		Shut down and discharge the stack voltage to less than 50% of the open circuit voltage

For the idle condition, the current was set at 66 A (200mA cm^{-2}), with the coolant temperature maintained at 65°C throughout the duration of the test. The gas stoichiometric ratios for H_2/air were 1.6/2.5. The inlet relative humidity (RH) was set at 45%RH/100%RH, with inlet pressures of 135kPa.a/120kPa.a. For the rated condition, the current was set at 495 A (1500 mA cm^{-2}), with the coolant temperature maintained at 70°C throughout the test. The gas stoichiometric ratios for H_2/air were 1.5/2.0, respectively. The inlet RH is set at 30%RH/65%RH for H_2/air, with inlet pressures of 215kPa.a/200kPa.a. For reference condition, the initial voltage is set at 0.7 V with a current of 462 A (1400 mA cm^{-2}), and the coolant temperature is maintained at 68°C. The gas stoichiometric ratios for H_2/air were 1.5/2.0. The inlet RH is set at 35%RH/70%RH for H_2/air, with inlet pressures of 215kPa.a/200kPa.a.

Table 2. AST procedure of rated condition.

Step	Condition	Parameters
1	Start	Precondition: Voltage of single cell < 0.3 V
		Maintained current: 66A
2	Idle	Holding time: 90s
3	Rated	Start timing
		Operating current: 495 A
		loading & unloading time: 35 s
4	Reference current	Unload from 495A to 462A at 1 hour intervals, hold for 90s and record voltage, then load to 495A
5	Stop	Precondition: 4h of continuous operation at 495A and 462A
		Idle holding time: 30s
		Shut down and discharge the stack voltage to less than 50% of the open circuit voltage

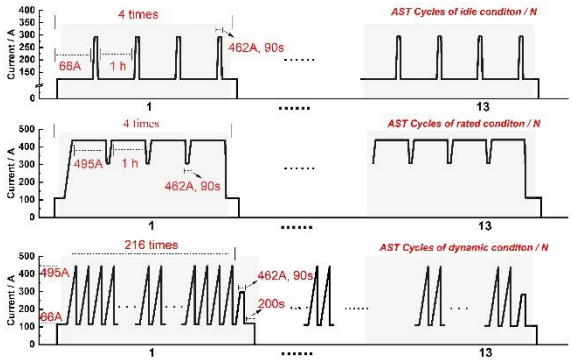

Fig.2 Current cycles diagram of accelerated stress test for different typical vehicle operating conditions, including Idle, Rated, Dynamic in order from top to bottom.

Table 3. AST procedure of dynamic condition.

Step	Condition	Parameters
1	Start	Precondition: Voltage of single cell < 0.3 V
		Maintained current: 66A
2	Idle	Holding time: 240s
3	Cyclic Variable Load	Start timing
		Loading amplitude:66A to 495 A
		Loading process: 30s
		Rated current time: 3s
		Unloading process 16s
		Unloading temination: 119A
		Idle current time: 15s
4	Reference current	Precondition: 216 completed cycles
		Load from 66A to 462A, hold for 90s and record voltage, then unload to 66A,hold for 200s
5	Stop	Shut down and discharge the stack voltage to less than 50% of the open circuit voltage

3. MODELS

3.1 CEEMDAN decomposition method

Complete Ensemble Empirical Mode Decomposition with Adaptive Noise (CEEMDAN) represents an enhancement to the Empirical Mode Decomposition (EMD) methodology. CEEMDAN addresses the issues of nonlinearity and non-stationarity by decomposing the original data set into intrinsic mode functions (IMFs) of varying frequencies. The incorporation of adaptive noise serves to eliminate the mode mixing issues that are inherent to the EMD process. In comparison to traditional EMD and its enhanced variants (e.g., EEMD, CEEMD), CEEMDAN introduces an additional signal-to-noise ratio to regulate the noise level throughout each decomposition process. This approach effectively mitigates the influence of white noise in the reconstruction outcomes, necessitating fewer iterations and demonstrating high decomposition efficiency [31].

The decomposition steps of CEEMDAN are referenced from the literature[30,31], and the specific steps are as follows:

Step1. Add white noise $w^i(t)\ (i = 1,2,3,\dots,n)$ with a signal-to-noise ratio ε_0 that follows a normal Gaussian distribution to the original voltage data $y(t)$. Then obtain the data $y^i(t)\ (i = 1,2,3,\dots,n)$, expressed as Eq. (1).

$$y^i(t) = y(t) + \varepsilon_0 w^i(t), i = 1,2,3,\dots,n \quad (1)$$

Step2， Perform EMD decomposition on $y^i(t)$ to obtain the first IMF sequence $IMF_1^i(t)$ for each of the n instances of $y^i(t)$， Finally, obtain the CEEMDAN decomposition sequence of the original voltage data according to Eq. (2), and obtain the first residual sequence according to Eq. (3).

$$IMF_1(t) = \frac{1}{n}\sum_{i=1}^{n} IMF_1^i(t) = \frac{1}{n} EMD_1\left(y^i(t)\right) \quad (2)$$

$$r_1(t) = y(t) - IMF_1(t) \quad (3)$$

Step3. Replace $y(t)$ in Eq. (1) with $r_1(t)$. The adaptive noise term is the first IMF of the white noise $w^i(t)$ from the EMD decomposition, with a signal-to-noise ratio of ε_1. Continue repeating Step 1 and Step 2 as shown in Eq. (4) and Eq. (5).

$$IMF_k = \frac{1}{n}\sum_{i=1}^{n} EMD_1\left(r_{k-1}(t) + \varepsilon_{k-1} EMD_{k-1}\left(w^i(t)\right)\right), \quad k = 2,3,\dots,K \quad (4)$$

$$r_k(t) = r_{k-1}(t) - IMF_k(t) \quad (5)$$

Step4. Repeat the above steps. Terminate the CEEMDAN algorithm when the residuals have no more than two extrema and can no longer be decomposed. The relationship for the original signal $y(t)$ is shown in Eq. (6).

$$y(t) = \sum_{k=1}^{K} IMF_k(t) + r_{K-1}(t) \quad (6)$$

where the nth IMF sequence equals the residual sequence $r_{K-1}(t)$.

3.2 Prediction model

Long Short-Term Memory (LSTM) alleviates the gradient vanishing problem of traditional Recurrent Neural Networks (RNN) by introducing gating structures. LSTM contains three key gates: forget gate, input gate and output gate. This gating mechanism allows the network to selectively memorize or forget information while processing sequential data, effectively learning long-term dependencies in time series, and is suitable for long data series prediction tasks.

The forget gate f_t determines which information in the history state is forgotten, and the forget gate can be expressed as Eq. (7).

$$f_t = \sigma\left(W_{xf}x_t + W_{hf}h_{t-1} + b_f\right) \quad (7)$$

The input gate i_t then determines which new information will be stored in the current state, which can be expressed as Eq (8). Based on the historical state output and the current input, the cell state can be calculated as shown in Eq. (9).

$$i_t = \sigma(W_{xi}x_t + W_{hi}h_{t-1} + b_i) \quad (8)$$

$$\tilde{c_t} = tanh(W_{xc}x_t + W_{hc}h_{t-1} + b_c) \quad (9)$$

At this point the current cell state c_t can be represented as Eq. (10), including the input gate point-by-point multiplication of history state and the forget gate point-by-point multiplication of Cell state $\tilde{c_t}$.

$$c_t = f_t \odot c_{t-1} + i_t \odot \tilde{c_t} \quad (10)$$

The output gate o_t determines the next hidden state. The output gate o_t and hidden state h_t are calculated as shown in Eq. (11) and Eq. (12).

$$o_t = \sigma(W_{xo}x_t + W_{ho}h_{t-1} + b_o) \quad (11)$$

$$h_t = o_t \odot tanh(c_t) \quad (12)$$

where W_{xi}, W_{xf} and W_{xo} are the weight matrices connected to the input x_t. W_{hi}, W_{hf} and W_{ho} are weight matrices connected to the output h_t. b_i, b_f, b_o represent the deviations of the corresponding gates.

In this study, the CEEMDAN method was employed for the decomposition of the voltage data into a total of n IMFs. Subsequently, each IMF component was predicted using an LSTM deep learning network. Ultimately, the prediction outcomes of all IMF components were aggregated to derive the final prediction result.

4. RESULTS AND DISCUSSION

4.1 Experimental results

Fig. 3 depicts the variation trends of stack voltage under Idle conditions. Fig. 3(a) shows the voltage degradation and subsequent recovery. Each AST cycle illustrated in Fig. 3(a) is comprised of four secondary cycles occurring within a four-hour period. It can be observed that within each secondary cycle, the voltage undergoes a gradual decline over a continuous period, with a decrease ranging from 0.2V to 0.5V. Following a brief alteration in load at 462A, a substantial recovery in voltage is observed. Within the first 8 hours, the voltage almost fully recovers, even surpassing the initial voltage of the previous secondary cycle. As the test duration is extended, the recovery between secondary cycles is observed to diminish. It is evident that brief load changes alone are insufficient to achieve full recovery. Furthermore, the overall voltage trend comprises multiple discrete segments, each comprising four or eight secondary cycles. These segments can be observed at the 8th, 12th, 24th, 28th, 32nd, 36th, and 44th hours. These segments are attributable to the implementation of overnight shutdown procedures. Following the cessation of operations during the night, the voltage demonstrates a notable recovery. However, the rates of decline in the initial secondary cycles following the overnight shutdown are also considerable. At the end of the 4th, 16th, 28th, 40th, and 48th hours, the system was terminated for one hour. As can be observed, a one-hour shutdown has a negligible effect on voltage recovery, with only a slight reduction in the rate of decline. This phenomenon may be attributed to a relatively dry internal condition of the stack at 66A. Following a brief load change at 462A, there was a temporary increase in water production, which resulted in voltage recovery. Moreover, the mean stack voltage at 66A is observed to fluctuate between 0.79V and 0.84V, which renders the Pt catalyst surface susceptible to oxidation. During shutdowns, the cathode voltage drops, and overnight resting allows partial reduction of the Pt oxide. Additionally, throughout the entire overnight shutdown, the water content within the ionomer of the MEA undergoes redistribution, accompanied by an increase in the dissolved water of the membrane material. Consequently, the voltage recovery is more pronounced following an overnight shutdown.

Fig. 3(b) illustrates the voltage variation trend under Rated condition. Unlike the Idle condition, there is no voltage recovery between secondary cycles. This is likely because the operational parameters at 495A are nearly identical to those at 462A, resulting in no significant change in water production and purging capability. Consequently, the voltage continuously declines. Both 1-hour shutdowns (e.g., at the 20th, 36th, and 44th hours) and overnight shutdowns (e.g., at the 8th, 12th, 16th, 24th, 32nd, 40th, and 48th hours) lead to significant voltage recovery. This suggests that, under the current parameters, shutdowns primarily aid in purging accumulated liquid water, improving gas transport. Within each AST cycle, the voltage decline trend shows inflection points with varying rates of decline, likely due to localized liquid water expulsion and accumulation during continuous operation.

Fig. 3(c) shows the voltage data under dynamic conditions. After the 40th and 48th hour, there was a

1hour shutdown before the next AST test, while other AST intervals involved overnight shutdowns. Both the voltages of 66A and 495A recover after shutdowns with similar trends. The voltage at 495A shows larger drops and recoveries, indicating that higher currents result in more pronounced voltage loss and recovery. Voltage trends at 495A also vary significantly, likely due to unstable internal water conditions and the random localized flooding and drainage within the stack.

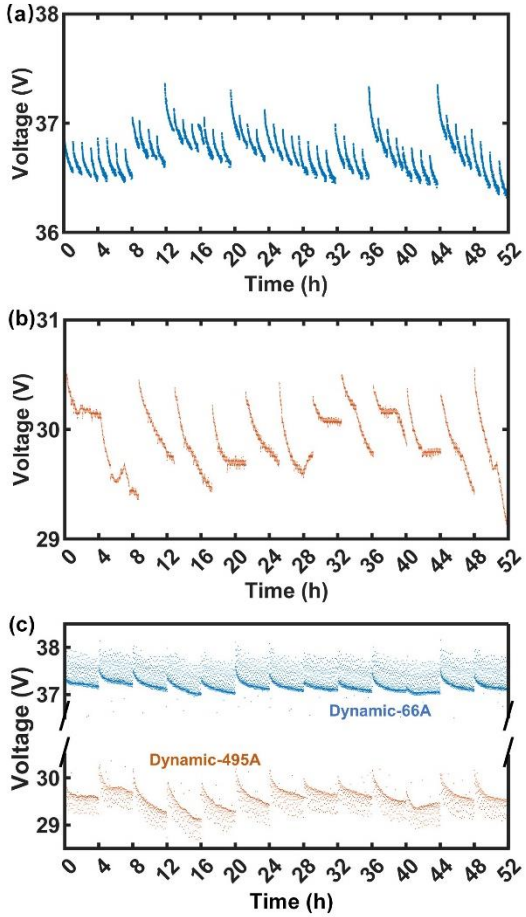

Fig.3 Voltage data from AST experiments: (a) Idle condition, (b) Rated condition, (c) Dynamic condition.

The consistency of the stack is a crucial performance indicator, reflecting the water content and relative degradation of each cell. In this study, we use the standard deviation of individual cell voltages, U_{std} , as the consistency metric, calculated as shown in Equation (13).

$$U_{std} = \sqrt{\frac{1}{N_{stack}-1}\sum_{m=1}^{N_{stack}}\left(V_m - \sigma_{avg}\right)^2} \qquad (13)$$

Where N_{stack} is the total number of individual cells in the stack, V_m is the voltage of $NO.m$ individual cell, and σ_{avg} is the average voltage of cells.

Fig. 4(a) depicts the U_{std} results for the stack under Idle and Rated conditions. The U_{std} under Rated conditions is consistently an order of magnitude higher than under Idle conditions. Furthermore, the U_{std} under rated conditions demonstrates an increase within each AST cycle, indicating a growing disparity in water content between individual cells, which subsequently decreases after shutdown recovery. Under Idle conditions, the Ustd predominantly remains below 0.004V, exhibiting a slight declining trend within each AST cycle, suggesting that the water content of each cell becomes increasingly consistent as they dry out over time.

Fig. 4(b) illustrates the typical results for varying currents under Dynamic conditions, exhibiting comparable patterns to those observed under Idle and Rated conditions. For 495A, U_{std} inversely correlates with voltage. Notably, the U_{std} for 66A is 2-3 times higher than under Idle conditions and decreases more rapidly. This suggests that the 66A consistency in Dynamic conditions is impacted by liquid water accumulation during 495A operation. This is evidenced by two points: first, the voltage at 66A under dynamic conditions is higher than under idle conditions, as shown in Fig. 3(a) and (b); second, the voltage trend at 66A aligns with that of 495A. Given that 66A should maintain sufficient humidity during each Dynamic AST, the differing voltage trends indicate that the brief 66A load (15s as mentioned in Table 3) is insufficient to remove all liquid water.

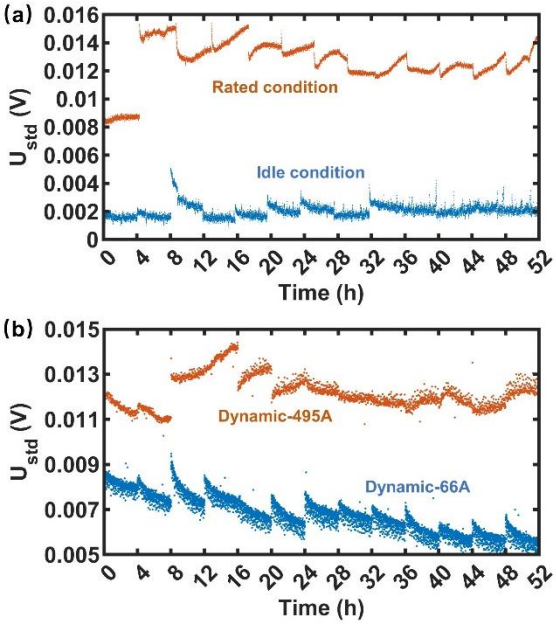

Fig.4 Consistency trend of the stack: (a) Idle condition and Rated condition, (b) Dynamic condition

4.2 *Voltage decomposition using CEEMDAN method*

During CEEMDAN decomposition, the standard deviation of the added noise was set to 20% of the signal's standard deviation. The signal was averaged 100 times, with a maximum of 5 iterations. For the Idle condition, this process yielded 14 IMFs and a residual, as shown in Fig. 5.

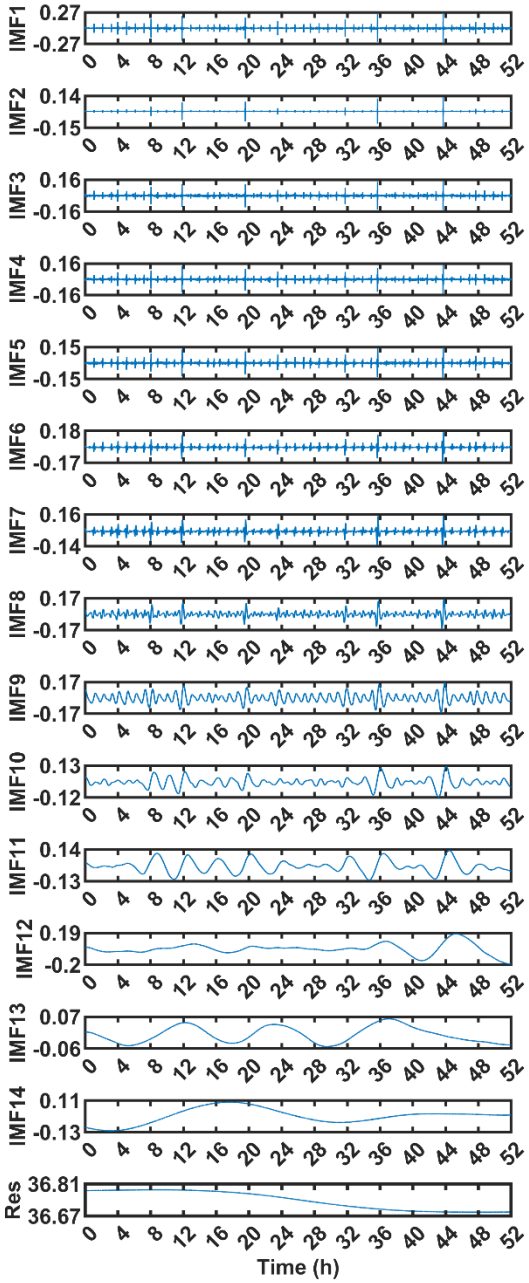

Fig. 5 CEEMDAN decomposition results of voltage data under Idle conditions.

The modes IMF1 to IMF14, which fluctuate around 0, are referred to as oscillatory components, whereas the relatively stable declining mode, Res, is designated as the trend component. The oscillatory components reflect recoverable fluctuations due to external factors and uncertainties, whereas the trend component indicates the irreversible voltage decline resulting from internal degradation over the course of long-term operation [30]. In idle conditions, the total 14 IMF sequences represent the periodic or abnormal influences on voltage decay across different aging time scales. The decline of the Res component from 36.81 to 36.67 serves to illustrate the primary aging trend. The nonlinear trends observed in IMF1-IMF14, with minor fluctuations, are indicative of internal state variations, external operating parameters change, and recoverable voltage losses. The periodic trends exhibited by IMF1 to IMF9 have a period of approximately one hour, with IMF9 displaying a particularly distinct pattern. These trends likely correlate with changes in each secondary cycle under idle conditions. IMF11 has a period close to four hours, matching the voltage recovery period observed in Fig. 3(a). The exact causes of the variations in other IMFs are still unclear. However, these IMF sequences likely reflect trends related to operational conditions during startup/shutdown cycles and localized recoverable phenomena.

Thus, CEEMDAN effectively preserves the dynamic factors affecting voltage decay by avoiding filtering of the raw data. It retains the uncertainty and periodic influences by converting the raw data into multiple modes. The voltage decompositions for Rated and Dynamic conditions are similar to that shown in Figure 5 and are not included in the main text.

4.3 *Voltage prediction results*

In this paper, the predictive performance of the model is evaluated using the root mean square error (RMSE) and the coefficient of determination (R^2). A smaller RMSE value indicates a higher level of prediction accuracy. A value of R^2 closer to 1 indicates a greater degree of alignment between the predicted and actual test results. The specific expressions are presented in Eq. (14) and Eq. (15):

$$RMSE = \sqrt{\frac{1}{m}\sum_{i=1}^{m}(y_i - \hat{y}_i)^2} \tag{14}$$

$$R^2 = 1 - \frac{\sum_{i=1}^{m}(y_i - \hat{y}_i)^2}{\sum_{i=1}^{m}(y_i - \overline{y}_i)^2} \tag{15}$$

where y_i is the actual raw stack voltage data, $\hat{y}_i$ is the predicted stack voltage data, $\overline{y}_i$ is the actual voltage average, and m is the number of stack voltage sampling points.

Prior to training with the proposed model, the raw voltage data from idle conditions was decomposed into multiple IMFs using CEEMDAN. Each IMF was then split into training (85%) and test (15%) sets to ensure ample training samples and reliable model assessment. This split ratio was also applied to rated and dynamic conditions. Subsequently, predictions were generated for each IMF component using the LSTM network, and these prediction results were combined to reconstruct the overall voltage predictions. The training phase was set with a maximum of 20 epochs, a mini-batch size of 25, and an initial learning rate of 0.001. The CEEMDAN-LSTM model used a time step of 3, predicting the next step's voltage based on the previous three measurements. It consisted of one input layer, one hidden layer with 3 units, and one output layer. The number of hidden units was carefully chosen to balance model learning and avoid overfitting.

Fig. 6 illustrates the voltage prediction results using the CEEMDAN-LSTM hybrid model for the idle condition, compared to the LSTM and GRU models. Table 4 presents the RMSE and R2 results for the test set. During the first two secondary cycles, the results of the CEEMDAN-LSTM model exhibit a slight divergence from those of the LSTM and GRU models. Nevertheless, the prediction results of all methods demonstrate a high degree of alignment with the actual voltage data. From the third to the fifth secondary cycles, predictions match the measured data well. Starting from the sixth secondary cycle (49h), at the end of each secondary cycle, significant divergences from actual voltage data are observed in all methods. In terms of the degree of correspondence between the model prediction results and the actual voltage data, the CEEMDAN-LSTM model outperforms the GRU model and the LSTM model. Furthermore, the differences among the three methods are more pronounced with longer running times and voltage degradation. Starting from the sixth secondary cycle, the prediction results of GRU model and LSTM model at the end of the secondary cycle remain almost the same, and it is difficult to follow the actual voltage trend. On the other hand, the prediction results of the CEEMDAN-LSTM model still fit the actual data better, although the degree of deviation also gradually increases. Compared with the LSTM model and the GRU model, the RMSE of the CEEMDAN-LSTM model is reduced by 30.41% and 18.21%, and the R^2 is improved by 1.62% and 1.09%, respectively. This can be attributed to the fact that the CEEMDAN method preserves the anomalous disturbances and periodic influences that cause voltage fluctuations during the test process, and these dynamic influences on short-term voltage fluctuations can help the network to obtain a better long-term prediction performance, which in turn improves the accuracy of the model predictions.

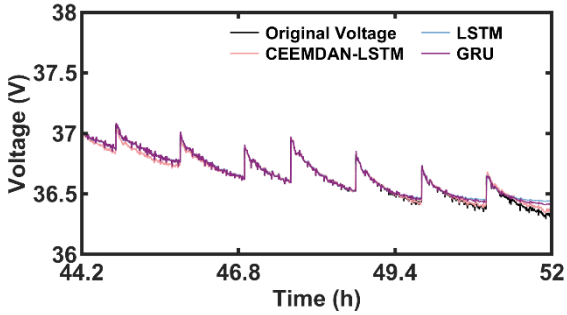

Fig.6 Prediction results of voltage under idle condition.

Fig. 7 shows the voltage prediction results at rated operating conditions. It can be seen that the prediction results of all three models are close to the actual voltage data up to the 50th hour. After 50 hours, however, the CEEMDAN-LSTM predictions begin to deviate very slightly from the actual voltage. At about the 51th hour, the LSTM and GRU model prediction results begin to deviate significantly from the actual voltage trend, with only the CEEMDAN-LSTM model prediction results being closest to the actual voltage data. Similar to the prediction results for the idle condition, the CEEMDAN-LSTM model still shows the best performance compared to the LSTM and GRU models. The RMSE of the CEEMDAN-LSTM model is reduced by 28.37% and 16.87%, and the R^2 is improved by 1.30% and 2.10% compared to the LSTM and GRU models, respectively. The prediction results of the CEEMDAN-LSTM model are more closely aligned with the actual voltage data, suggesting that the hybrid CEEMDAN-LSTM model's performance in predicting highly nonlinear data features is markedly superior to that of the individual methods.

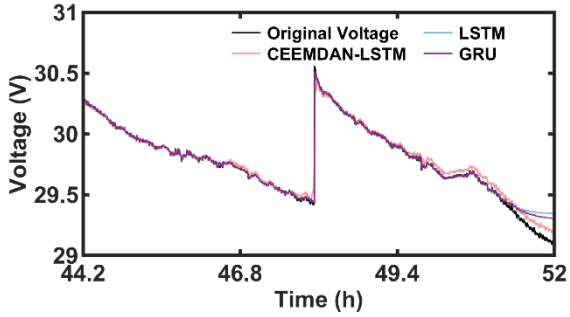

Fig.7 Prediction results of voltage under rated condition.

Given that the PEMFC stack is in constant-current steady-state operation under idle and rated conditions, this paper further investigated the performance of the proposed CEEMDAN-LSTM model under Dynamic condition. Fig. 8 and Table 4 show the prediction results under dynamic condition. Compared with the LSTM

model and the GRU model, the RMSE of the CEEMDAN-LSTM model is reduced by 17.02% and 16.14%, and the R^2 is improved by 1.36% and 1.28%, respectively. These results demonstrate the CEEMDAN-LSTM model's robust predictive performance for both steady-state and dynamic conditions with complex voltage trends.

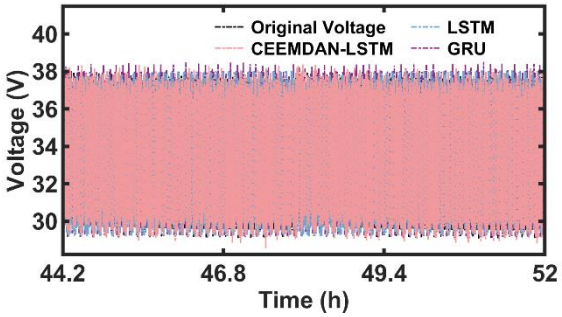

Fig.8 Prediction results of voltage under dynamic condition.

Table 4. Comparison of results of different prediction methods for various operating conditions.

Conditions	Models	RSME-Test	R^2-Test	Increase-RSME	Increase-R^2
Idle	LSTM	0.0342	0.9762	30.41%	1.62%
	GRU	0.0291	0.9813	18.21%	1.095
	CEEMDAN-LSTM	0.0238	0.992	/	/
Rated	LSTM	0.0564	0.971	28.37%	2.10%
	GRU	0.0486	0.9787	16.87%	1.30%
	CEEMDAN-LSTM	0.0404	0.9914	/	/
Dynamic	LSTM	0.6157	0.9588	17.02%	1.36%
	GRU	0.6092	0.9595	16.14%	1.28%
	CEEMDAN-LSTM	0.5109	0.9718	/	/

5. CONCLUSIONS

This study evaluated a 15kW fuel cell stack under Idle, Rated, and Dynamic load conditions through accelerated stress testing to assess performance recovery after shutdowns. Results demonstrate significant voltage recovery across all currents, with the most pronounced reversible loss and recovery under high currents. The consistency of the stack is more variable at higher currents, showing an inverse relationship with voltage's reversible decay. Additionally, a data-driven model combining CEEMDAN and LSTM networks was proposed. CEEMDAN decomposes voltage data into dynamic factors that enhance neural network training. The CEEMDAN-LSTM model reduced RMSE by 30.41% and 18.21% compared to LSTM and GRU models under idle conditions, by 28.37% and 16.87% under rated conditions, and by 17.02% and 16.14% under dynamic conditions.

ACKNOWLEDGEMENT

This work was supported by The National Natural Science Foundation of China (52077157), the Fundamental Research Funds for the Central Universities (22120240289), National Key Research and Development Program of China (2023YFB4301604), and National Key Research and Development Program of China (2023YFB4301603).

REFERENCE

[1] Shao Y, Xu L, Hu Z, Xu L, Jia X, Zhang X, et al. New insights into steady-state multiplicity in polymer electrolyte membrane fuel cell. J Power Sources 2023;554:232328.

[2] Mitzel J, Zhang Q, Gazdzicki P, Friedrich KA. Review on mechanisms and recovery procedures for reversible performance losses in polymer electrolyte membrane fuel cells. J Power Sources 2021;488:229375.

[3] Pei P, Chang Q, Tang T. A quick evaluating method for automotive fuel cell lifetime. Int J Hydrog Energy 2008;33:3829–36.

[4] Cleghorn SJC, Mayfield DK, Moore DA, Moore JC, Rusch G, Sherman TW, et al. A polymer electrolyte fuel cell life test: 3 years of continuous operation. J Power Sources 2006;158:446–54.

[5] Jahromi MM, Heidary H. Durability and economics investigations on triple stack configuration and its power management strategy for fuel cell vehicles. Int J Hydrog Energy 2021;46:5740–55.

[6] Zhang X, Pisu P. Prognostic-oriented Fuel Cell Catalyst Aging Modeling and Its Application to Health-Monitoring and Prognostics of a PEM Fuel Cell. Int J Progn Health Manag 2020;5.

[7] Kabasawa A, Saito J, Miyatake K, Uchida H, Watanabe M. Effects of the decomposition products of sulfonated polyimide and Nafion membranes on the degradation and recovery of electrode performance in PEFCs. Electrochimica Acta 2009;54:2754–60.

[8] Jomori S, Komatsubara K, Nonoyama N, Kato M, Yoshida T. An Experimental Study of the Effects of Operational History on Activity Changes in a PEMFC. J Electrochem Soc 2013;160:F1067–73.

[9] Kreitmeier S, Michiardi M, Wokaun A, Büchi FN. Factors determining the gas crossover through pinholes in polymer electrolyte fuel cell membranes. Electrochimica Acta 2012;80:240–7.

[10] Gazdzick P, Mitzel J, Garcia Sanchez D, Schulze M, Friedrich KA. Evaluation of reversible and irreversible

degradation rates of polymer electrolyte membrane fuel cells tested in automotive conditions. J Power Sources 2016;327:86–95.
[11] Nguyen TV, Knobbe MW. A liquid water management strategy for PEM fuel cell stacks. J Power Sources 2003;114:70-9.
[12] Schulze M, Wagner N, Kaz T, Friedrich KA. Combined electrochemical and surface analysis investigation of degradation processes in polymer electrolyte membrane fuel cells. Electrochimica Acta 2007;52:2328–36.
[13] Pivac I, Barbir F. Impact of Shutdown Procedures on Recovery Phenomena of Proton Exchange Membrane Fuel Cells. Fuel Cells 2020;20:185–95.
[14] Zhang S, Yuan X-Z, Hin JNC, Wang H, Wu J, Friedrich KA, et al. Effects of open-circuit operation on membrane and catalyst layer degradation in proton exchange membrane fuel cells. J Power Sources 2010;195:1142–8.
[15] Moein-Jahromi M, Kermani MJ, Movahed S. Degradation forecast for PEMFC cathode-catalysts under cyclic loads. J Power Sources 2017;359:611–25.
[16] Jha MS, Dauphin-Tanguy G, Ould-Bouamama B. Particle filter based hybrid prognostics for health monitoring of uncertain systems in bond graph framework. Mech Syst Signal Process 2016;75:301–29.
[17] Zhou D, Wu Y, Gao F, Breaz E, Ravey A, Miraoui A. Degradation Prediction of PEM Fuel Cell Stack Based on Multiphysical Aging Model With Particle Filter Approach. IEEE Trans Ind Appl 2017;53:4041–52.
[18] Liu H, Chen J, Hissel D, Lu J, Hou M, Shao Z. Prognostics methods and degradation indexes of proton exchange membrane fuel cells: A review. Renew Sustain Energy Rev 2020;123:109721.
[19] Liu H, Chen J, Hissel D, Su H. Remaining useful life estimation for proton exchange membrane fuel cells using a hybrid method. Appl Energy 2019;237:910–9.
[20] Bressel M, Hilairet M, Hissel D, Ould Bouamama B. Extended Kalman Filter for prognostic of Proton Exchange Membrane Fuel Cell. Appl Energy 2016;164:220–7.
[21] Bao C, Ouyang M, Yi B. Modeling and control of air stream and hydrogen flow with recirculation in a PEM fuel cell system—II. Linear and adaptive nonlinear control. Int J Hydrog Energy 2006;31:1897–913.
[22] Zhou S, Lu Y, Bao D, Wang K, Shan J, Hou Z. Real-time data-driven fault diagnosis of proton exchange membrane fuel cell system based on binary encoding convolutional neural network. Int J Hydrog Energy 2022;47:10976–89.
[23] Zuo J, Lv H, Zhou D, Xue Q, Jin L, Zhou W, et al. Deep learning based prognostic framework towards proton exchange membrane fuel cell for automotive application. Appl Energy 2021;281:115937.
[24] Yang Y, Yang Y, Zhou S, Li H, Zhu W, Liu Y, et al. Degradation prediction of proton exchange membrane fuel cell based on mixed gated units under multiple operating conditions. Int J Hydrog Energy 2024;67:268–81.
[25] Kheirandish A, Shafiabady N, Dahari M, Kazemi MS, Isa D. Modeling of commercial proton exchange membrane fuel cell using support vector machine. Int J Hydrog Energy 2016;41:11351–8.
[26] He K, Mao L, Yu J, Huang W, He Q, Jackson L. Long-Term Performance Prediction of PEMFC Based on LASSO-ESN. IEEE Trans Instrum Meas 2021;70:1–11.
[27] Ma T, Liang Y, Cong M, Yao N, Wang K. Remaining Useful Life Prediction Based on LSTM with Peephole for PEMFC, 2022, p. 2022-01–7037.
[28] Sun B, Liu X, Wang J, Wei X, Yuan H, Dai H. Short-term performance degradation prediction of a commercial vehicle fuel cell system based on CNN and LSTM hybrid neural network. Int J Hydrog Energy 2023;48:8613–28.
[29] Ibrahim M, Steiner N, Jemei S, Hissel D. Wavelets-based approach for online Fuel Cells Remaining Useful lifetime Prediction. IEEE Trans Ind Electron 2016:1–1.
[30] Li C, Lin W, Wu H, Li Y, Zhu W, Xie C, et al. Performance degradation decomposition-ensemble prediction of PEMFC using CEEMDAN and dual data-driven model. Renew Energy 2023;215:118913.
[31] Zhou F, Huang Z, Zhang C. Carbon price forecasting based on CEEMDAN and LSTM. Appl Energy 2022;311:118601.